Research Article

ADVANCED PHOTONICS NEXUS

Nonlinear virtual lens for programmable and multispectral infrared upconversion imaging

Ze Zheng,[a] Olga Sergaeva,[b] Davide Rocco,[b,c] Yuchen Zhang,[d] Guoquan Zhang,[d] Mohsen Rahmani,[a,*] Costantino De Angelis,[b,c,*] and Lei Xu[a,*]

[a]Nottingham Trent University, School of Science & Technology, Advanced Optics and Photonics Laboratory, Department of Engineering, Nottingham, United Kingdom
[b]University of Brescia, Department of Information Engineering, Brescia, Italy
[c]National Institute of Optics, Consiglio Nazionale delle Ricerche, Brescia, Italy
[d]Nankai University, TEDA Applied Physics Institute and School of Physics, The MOE Key Laboratory of Weak Light Nonlinear Photonics, Tianjin, China

Abstract. Conventional infrared (IR) imaging techniques depend on IR cameras based on narrow-bandgap semiconductors, which offer limited spectral bandwidth. Recently, advances in nonlinear flat optics have opened a pathway for converting IR signals into the visible through nonlinear generations, enabling the direct visualization of IR images using standard visible cameras. However, the narrow spectral bandwidth remains a key challenge. We address both issues via an adaptive and multifunctional IR-to-visible imaging platform offering tunable bandwidth and focusing simultaneously. We utilize sum-frequency generation (SFG) to convert IR light into the visible by introducing a pump beam modulated by a spatial light modulator (SLM) to construct a virtual metalens enabling precisely controlled focusing of the generated nonlinear optical field. As a result, we demonstrate both theoretically and experimentally an optical focusing mechanism with a tunable focal length, achieved by varying the pump and signal wavelengths and modulating the phase distribution. Furthermore, because the focal length depends on the input signal wavelength, the imaging plane position varies accordingly, indicating a promising potential for the multispectral IR imaging applications. Our upconversion platform delivers SLM-controlled, programmable multispectral focusing for next-generation IR imaging, opening new avenues in the fields of computational and multispectral imaging techniques.

Keywords: flat optics; spatial light modulator; nonlinear optics; multispectral imaging.

Received Jan. 14, 2026; accepted for publication May 27, 2026; published online Jun. 23, 2026.

[DOI: 10.1117/1.APN.5.4.046024]

1 Introduction

Infrared (IR) imaging has become a cornerstone technology for modern industry, enabling applications in medicine,[1] sensing,[2] night vision,[3,4] and building inspection.[5] The conventional detection techniques of IR light rely on the use of IR cameras. However, IR cameras typically provide lower spatial resolution than visible sensors,[6] lack color information,[4] and increase the system cost,[6] particularly as cryogenic cooling is required for many IR cameras to improve their sensitivity.[7] Moreover, traditional IR cameras rely on narrow-bandgap semiconductors, meaning that a given IR camera is sensitive only to a specific spectral range and cannot cover the entire IR range, as efficient IR photon detection is constrained by the semiconductor bandgap.[8] These constraints motivate the development of nonlinear frequency-conversion approaches that can translate IR information into the visible, enabling IR detection with conventional visible cameras leveraging the strengths of both systems.[9–12]

One of the fundamental processes in nonlinear optics, nonlinear frequency conversion, is the physical process by which light at fundamental optical frequencies generates coherent output at the sum or difference frequencies within nonlinear materials, including sum-frequency generation (SFG) and its

*Address all correspondence to Mohsen Rahmani, mohsen.rahmani@ntu.ac.uk; Costantino De Angelis, costantino.deangelis@unibs.it; Lei Xu, lei.xu@ntu.ac.uk

degenerate case, second-harmonic generation (SHG), and higher-order processes such as four-wave mixing (FWM).[13,14] A wide range of platforms for such nonlinear optical processes has been extensively studied, including bulk nonlinear crystals,[13,15] optical fibers,[16,17] and integrated waveguides.[18,19] Among these, satisfying the phase-matching (momentum-conservation) condition is essential for efficient generation,[14,17,20] but it also restricts operation to a relatively narrow spectral bandwidth and specific wave-vector (propagation) configurations of the input waves.[21] These constraints substantially limit the practical use of these conventional platforms.

Flat-optical platforms (including nonlinear metasurfaces) relax the conventional phase-matching constraints for efficient nonlinear generation.[22–24] Unlike bulk crystals, fibers, or waveguides, where one balances dispersion over millimeter- to centimeter-scale interaction lengths, the physical thickness in flat optics is typically subwavelength.[22] Consequently, the accumulated phase-mismatch term Δkd (with Δk the phase mismatch and d the propagation distance) remains $\ll 1$ and can often be neglected.[25,26] This ultrathin platform supports broadband, angle-tolerant nonlinear generation,[25,26] which has broadened the application space of flat optics, including optical data processing,[27–30] optical computing,[29,31] and infrared imaging.[9–12]

Recently, the IR imaging technique based on nonlinear generation has been demonstrated with visible cameras in combination with nonlinear metasurfaces[9,11,12] and nanowire arrays.[32] In these systems, IR scenes are efficiently upconverted to the visible, enabling conventional visible cameras to perform IR detection. Notably, broadband IR imaging via FWM has been achieved, highlighting the advantages of flat-optical platforms for imaging.[12] On the contrary, there is a growing need to adapt in real time to scene dynamics and system fluctuations, enabling rapid aberration correction,[33–35] dynamic focusing,[36,37] and agile beam steering.[38,39] Real-time reconfigurable wavefront control has become both essential and challenging. Spatial light modulators (SLMs), which dynamically manipulate phase and amplitude in a two-dimensional pixel array, have emerged as powerful tools for agile wavefront engineering.[36,40] SLM-driven optical systems are now widely used in various domains, including computational imaging,[41,42] focusing through random scattering media,[43] and physical computing.[44,45]

In this work, we propose a virtual lens platform based on the SFG process that combines IR lensing and imaging together, achieving real-time programmable lensing and multispectral IR imaging via nonlinear generation in a thin lithium niobate film. Using an SLM to encode the real-time phase profile onto a pump beam, we demonstrate dynamically tunable IR focusing and imaging that can be directly captured by visible cameras, as shown in the schematic diagram (Fig. 1). A 600-nm-thick lithium niobate (LN, $LiNbO_3$) film serves as the nonlinear platform converting IR signals to the visible. A collimated Gaussian signal beam carries imaging information. We imprint a Fresnel zone lens (FZL) phase onto the pump beam with the SLM, which introduces the SFG interaction and induces nonlinear focusing of the SFG emission. Consequently, a signal beam at near-infrared region that carries imaging information is upconverted and recorded by a standard visible camera. As the effective focal length depends on the wavelengths of both the signal and the pump, the imaging plane shifts when tuning these wavelengths, thereby enabling multispectral imaging within the same architecture. Our approach opens a new avenue for programmable, multispectral infrared imaging based on nonlinear generation, advancing the applications of nonlinear imaging and wavefront shaping.

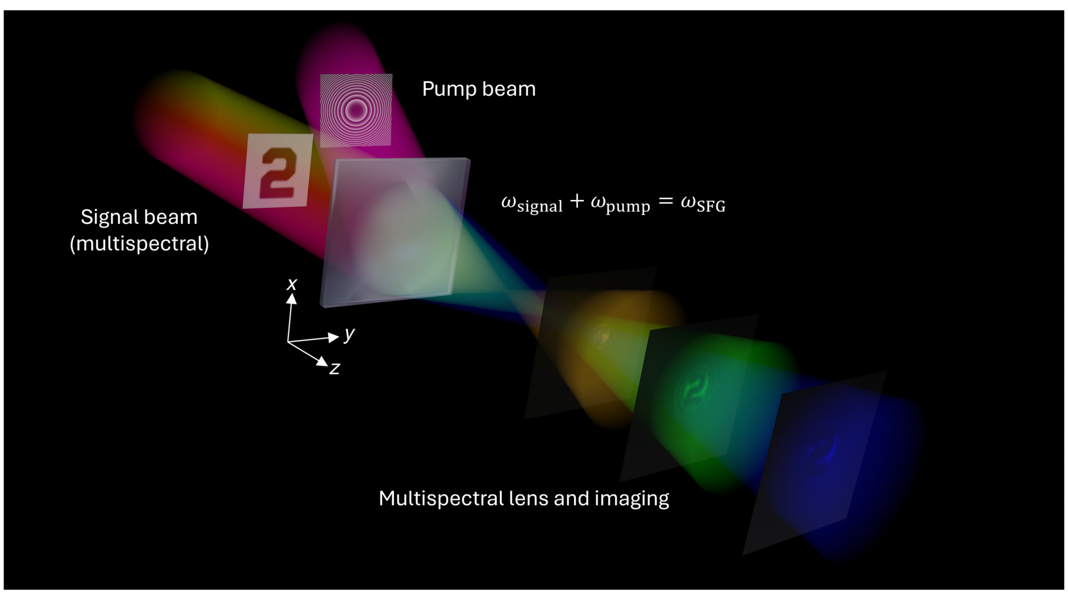

Fig. 1 Schematic illustrates our dynamic IR focusing and imaging technique based on SFG with a visible camera and an SLM. The number “2” in the signal arm marks the imaging target. In the pump arm, the FZL phase, modulated via the SLM, provides the required phase distribution. The yellow, green, and purple light cones denote SFG emission at different wavelengths corresponding to different pump wavelengths, which focus at distinct focal lengths. Consequently, image planes corresponding to different wavelengths are formed at different axial positions.

2 Results

We begin by introducing the concept of nonlinear lensing with an idealized theoretical model. First, an ultrathin lithium niobate film is utilized as the second-order nonlinear medium.[46–48] For simplicity, we ignore the light longitudinal propagation within the film and phase-matching effects due to the negligible thickness of our film. The generated SFG and SHG intensities are estimated by treating the LN film as a sheet of second-order polarization, as described by the following equation[14,49]:

$$P_i^{(2)}(\omega_1+\omega_2) = 2\varepsilon_0 \sum_{j,k} d_{ijk} E_j(\omega_1) E_k(\omega_2), \tag{1}$$

where ε_0 is the vacuum permittivity, $P_i^{(2)}$ is the i'th Cartesian component of the second-order nonlinear polarization, $E_j(\omega_1)$ and $E_k(\omega_2)$ are the Cartesian components of the incident electric fields (for SFG: $\omega_1 = \omega_{\text{pump}}$, $\omega_2 = \omega_{\text{signal}}$; for SHG: $\omega_1 = \omega_2 = \omega_{\text{pump}}$), and d_{ijk} are the elements of the second-order nonlinear tensor. The entire system is defined in a Cartesian coordinate system: the x- and y-directions lie in the film plane, and the z-direction is normal to the lithium niobate film.

We consider a 1550-nm pump beam whose optical axis is normal to the lithium niobate film. An FZL phase distribution is encoded at the SLM plane and projected onto the film plane through a $4f$ system and is defined by:

$$\phi_{\text{cont}}(x,y) = \text{mod}\left(\frac{2\pi}{r_1^2}(x^2+y^2), 2\pi\right) = 2\pi\text{frac}\left(\frac{x^2+y^2}{r_1^2}\right), \tag{2}$$

where $\text{frac}(x) = x - \lfloor x \rfloor$ denotes the fractional part, $\text{mod}(a, 2\pi)$ wraps the phase into $[0, 2\pi)$, and r_1 is the radius of the first half-wave FZL zone. The phase distribution at the film plane enables the focusing of the pump beam with the focal length, which can be calculated as[50]

$$f_{\text{FZL}} = \frac{r_1^2}{2\lambda_{\text{pump}}} = \frac{(n_{\min} p f_2/f_1)^2}{2\lambda_{\text{pump}}}. \tag{3}$$

A collimated Gaussian signal beam is also introduced with normal incidence on the lithium niobate film. $LiNbO_3$, as a second-order nonlinear medium, with the pump and signal incidences, supports three nonlinear optical processes arising from the pump and signal interactions: two SHG ($\omega_{\text{SHGs}} = 2\omega_{\text{signal}}$ and $\omega_{\text{SHGp}} = 2\omega_{\text{pump}}$) and one SFG ($\omega_{\text{SFG}} = \omega_{\text{signal}} + \omega_{\text{pump}}$). Among these, nonlinear focusing occurs in processes involving the pump beam because the FZL phase is transferred by the pump field. The SHG process $\omega_{\text{SHGs}} = 2\omega_{\text{signal}}$ will not be discussed further, as it does not exhibit focusing behavior. In this work, we primarily investigate the SHG induced by the pump beam ($\omega_{\text{SHGp}} = 2\omega_{\text{pump}}$) and the SFG induced by both pump and signal beams ($\omega_{\text{SFG}} = \omega_{\text{signal}} + \omega_{\text{pump}}$). Unless stated otherwise, throughout the discussion, the term "SHG" used below specifically refers to the pump-induced second-harmonic process ($\omega_{\text{SHGp}} = 2\omega_{\text{pump}}$).

The optical setup used to realize the theoretical model above is illustrated in Fig. 2. Two femtosecond lasers provide the signal and pump beams. The signal beam passes sequentially through a beam splitter (BS), lens 1, lens 2, and the lithium niobate film, where, in the presence of the pump, it contributes to SFG. The pump beam enters the BS along a different path, is directed to and reflected by the SLM, and then returns to the BS, where it is combined with the signal. After beam combination, the pump follows the same optical path (from lens 1, lens 2 to the lithium niobate film) and, within the film, interacts to generate the nonlinear signals. After spectrally filtering out the pump and signal beams, the generated nonlinear emission is collected by a 20× objective and detected by a CMOS camera. The SLM modulates the pump beam by imposing an FZL phase distribution, which is projected to the lithium niobate film through a $4f$ imaging system formed by the SLM, lens 1, and lens 2. The objective is mounted on a computer-controlled electric motion stage. The 3D intensity distributions of the optical field are measured by moving the motion stage as well as the objective.

The relationship between the induced nonlinear polarization of SFG and the signal and pump electric fields can be simplified as $\mathbf{P}^{\text{SFG}}(\omega_{\text{signal}} + \omega_{\text{pump}}) \propto \chi^{(2)} : [\mathbf{E}(\omega_{\text{signal}})\mathbf{E}(\omega_{\text{pump}})]$, where $\chi^{(2)}$ is the second-order nonlinear susceptibility tensor of lithium niobate, and ":" denotes a double contraction over the field indices. Based on SFG, the phase and amplitude distributions of the pump and signal can be transferred via this relationship, thus determining the nonlinear wavefront. Here, we modulate the pump beam with an FZL phase distribution, allowing it to be transferred to the nonlinear emissions and thus enabling its nonlinear focusing. Based on Eq. (3), the focal length of the SFG focusing with the projection of the $4f$ system can be calculated using

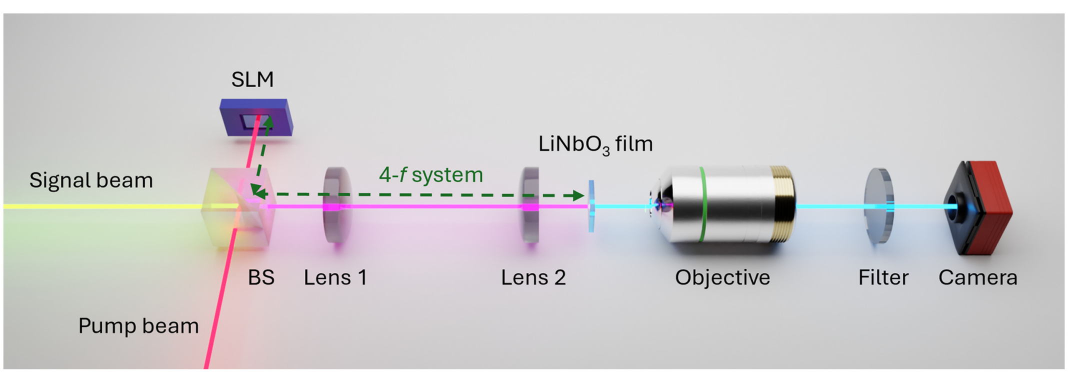

Fig. 2 Schematic shows the optical setup used to achieve and measure the IR focusing and imaging (BS is the 50:50 beam splitter).

$$f_{\mathrm{FZL,SFG}} = \frac{(n_{\min} p f_2/f_1)^2}{2\lambda_{\mathrm{SFG}}}, \tag{4}$$

where $n_{\min}$ is the pixel number of the first half-wave FZL zone, $p = 4.5\ \mu\mathrm{m}$ is the pixel pitch of the SLM, and $f_1 = 150$ mm and $f_2 = 30$ mm are the focal lengths of lens 1 and lens 2 in the $4f$ system, respectively.

Although the SHG focusing slightly varies from the SFG focusing, due to the quadratic relationship between the SHG polarization and the pump electric field, which can be expressed as the equation $\mathbf{P}^{\mathrm{SHG}}(2\omega_{\mathrm{pump}}) \propto \chi^{(2)} : [\mathbf{E}(\omega_{\mathrm{pump}})\mathbf{E}(\omega_{\mathrm{pump}})]$. The quadratic relationship results in the FZL phase distribution being transferred to the SHG signal twice, and therefore, the corresponding focal length must be reduced by a factor of two:

$$f_{\mathrm{FZL,SHG}} = \frac{1}{2}\frac{(n_{\min} p f_2/f_1)^2}{2\lambda_{\mathrm{SHG}}}. \tag{5}$$

We then simulate the nonlinear focusing via modeling the nonlinear electric field using the angular spectrum method (Fourier-domain free-space propagation). The nonlinear polarization is treated as an effective zero-thickness sheet at the film coordinate, determined by the lithium niobate second-order nonlinear tensor. The detailed information regarding the simulation can be found in Sec. I in the Supplementary Material.

The comparison between the simulated and measured optical fields of SHG and SFG focusing is exhibited in Fig. 3. Here, a signal beam with a central wavelength of 1100 nm and a pump beam with a central wavelength of 1550 nm are introduced, thus generating the SHG and SFG fields at 775 and 643 nm, consequently. The simulated and experimental optical patterns are in good agreement. In the simulation, where the SHG is generated at a single plane and propagated in free space, the quadratic phase transfer results in the SHG and pump fields focusing at the same axial position.

The focal length of the simulated [Fig. 3(a)] and measured [Fig. 3(b)] SHG focusing is 4.1 mm. The focal length of the SFG focusing in Fig. 3 is 9.7 mm for both simulation [Fig. 3(c)] and

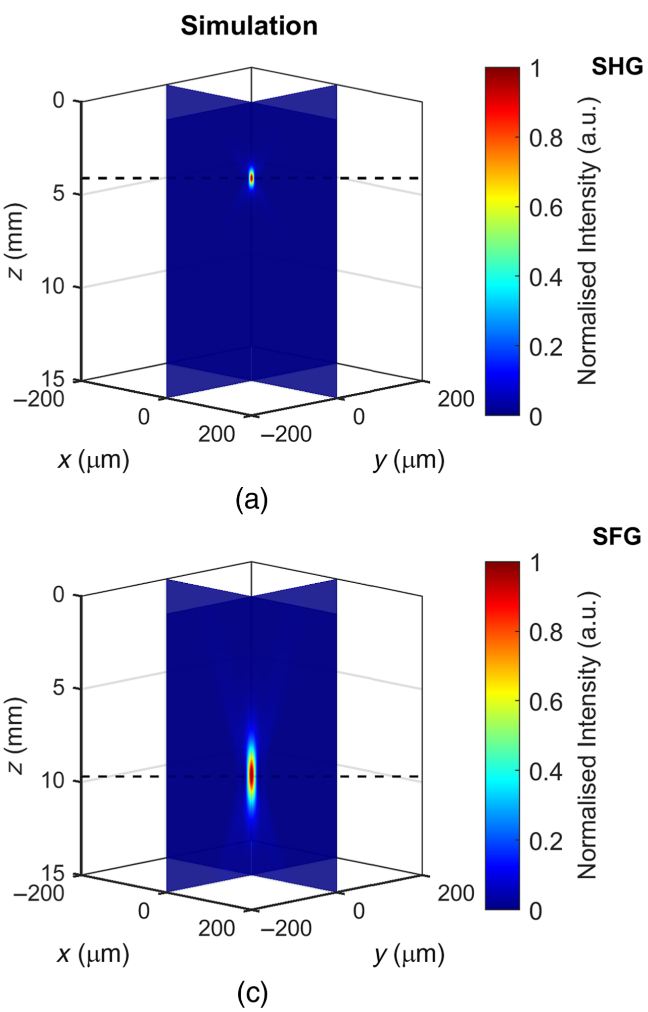

Fig. 3 Simulated (a), (c) and measured (b), (d) 3D optical fields of the SHG (a), (b) and SFG (c), (d) focusing with the signal wavelength at 1100 nm and the pump wavelength at 1550 nm. The first half-wave zone has a radius of 120 pixels on the SLM in the FZL phase pattern. The normalized intensity exhibits the relative distribution within one optical field, but it does not capture absolute intensity differences across differently focused optical fields.

experiment [Fig. 3(d)]. Moreover, the SFG focal length is almost twice that of the SHG focal length. Given that the SHG and SFG wavelengths are relatively close ($\lambda_{\mathrm{SHG}} = 775$ nm; $\lambda_{\mathrm{SFG}} = 643$ nm) compared with the observed difference in focal lengths, this behavior demonstrates that the nonlinear interaction governs the transfer of the phase distribution. In particular, it confirms that an additional factor of one-half must be included when predicting the SHG focal length.

According to Eq. (3), the focal length can be manipulated by tuning the phase distribution and the wavelength. Here, the pixel number refers to the number of SLM pixels defining the radius of the first half-wave Fresnel zone in the FZL phase pattern. We first tune the phase distribution by changing the pixel number of the first half-wave FZL zone and then observe the resulting SHG and SFG focusing at different focal lengths (Fig. 4 and Sec. II in the Supplementary Material). Experimentally, we observe that increasing the pixel number leads to longer focal lengths, for both the SHG [Figs. 4(a), 4(c), and 4(e)] and SFG [Figs. 4(b), 4(d), and 4(f)], in agreement with the theoretical prediction.

The focal plane of the SFG emission is determined by both the pump and signal wavelengths. Figures 5(a)–5(c) and Sec. III in the Supplementary Material illustrate that the SFG focal length decreases from 12.2 to 9.3 mm as the signal wavelength is tuned from 800 to 1200 nm. This occurs because each signal wavelength, when combined with a fixed pump wavelength, produces a distinct SFG wavelength and therefore a different focal length. According to Eq. (4), the focal length and the wavelength are inversely proportional; consequently, the focal length decreases as the signal wavelength increases. The theoretical focal lengths calculated from Eq. (4) are compared with the measured values in Fig. 5(d). In the experiment, finite film and substrate thicknesses introduce a small axial shift. To compensate for offsets arising from the LN film thickness (600 nm) and the substrate (1 mm), we apply a constant shift $\Delta_{\mathrm{sfg}} = 40$ nm to the SFG wavelength axis for the theoretical curves only. The measured focal lengths agree closely with the adjusted calculation. The residuals between the theoretical and experimental focal lengths are shown in Fig. 5(e).

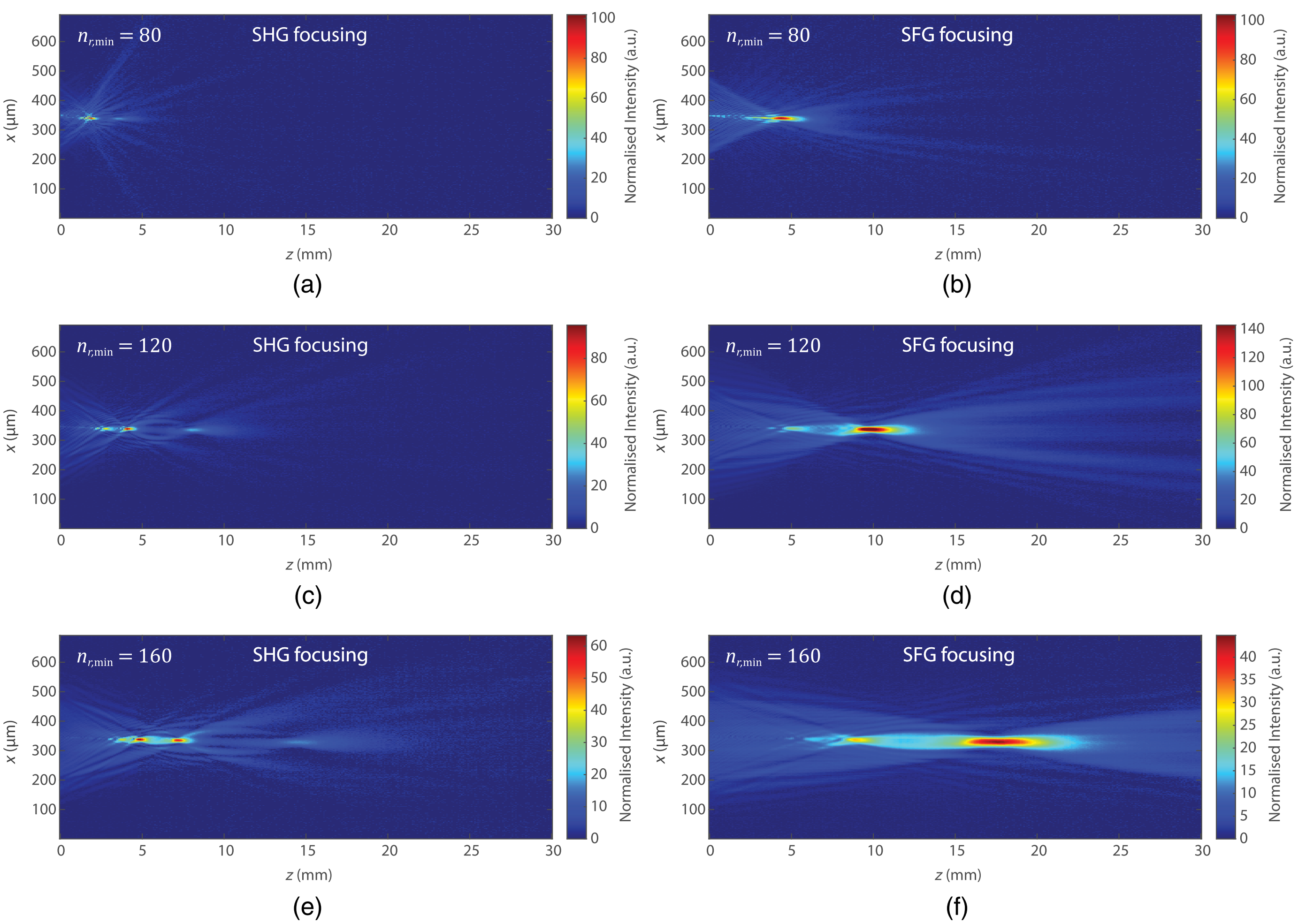

Fig. 4 Measured intensity distributions of the optical field in the xz plane of the SHG (a), (c), (e) and SFG (b), (d), (f) focusing for first half-wave-zone radii of 80, 120, and 160 pixels on the SLM in the FZL phase pattern: (a), (b) 80 pixels, (c), (d) 120 pixels, and (e), (f) 160 pixels. The signal wavelength and pump wavelength are fixed at 1100 and 1550 nm, respectively. The intensity was obtained from camera photon counts, corrected for background and normalized by the exposure time, and is therefore shown in relative units. The color scale is chosen to optimize overall visibility in each subfigure. As a result, the focal region may appear saturated.

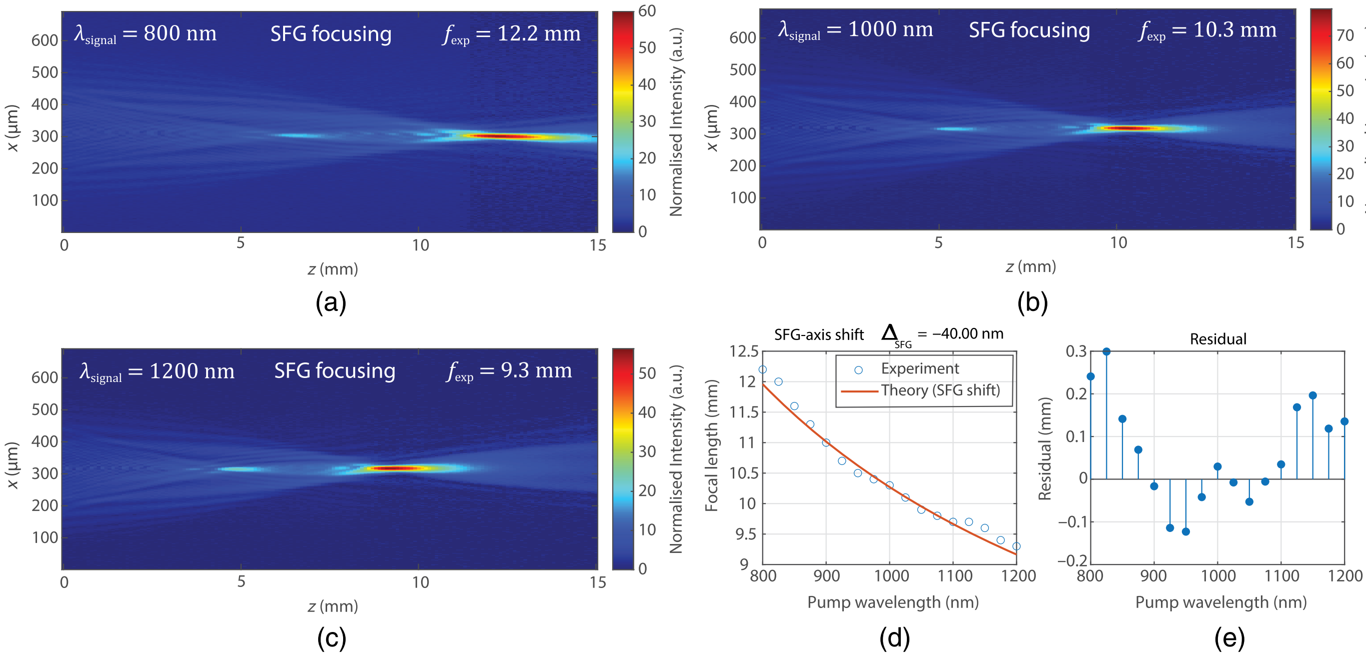

Fig. 5 Measured intensity distributions of the optical field in the xz plane of the SFG focusing with the signal wavelengths at 800 (a), 1000 (b), and 1200 nm (c), and the pump wavelength at 1550 nm. The measured focal lengths are shown in the top right corner of panels (a)–(c). The first half-wave zone has a radius of 120 pixels on the SLM in the FZL phase pattern. The intensity was obtained from camera photon counts, corrected for background and normalized by the exposure time, and is therefore shown in relative units. The color scale is chosen to optimize overall visibility in each subfigure. As a result, the focal region may appear saturated. (d) Focal length versus pump wavelength, experiment, and theory [Eq. (4)], with an SFG-axis shift applied to the theory only. Measured focal length (points, mm) is plotted against the pump wavelength and compared with the FZL prediction (line). A constant shift Δ_{sfg} is added only to the theoretical SFG wavelength according to Eq. (4) ($\lambda_{sfg} + \Delta_{sfg}$). (e) Residuals $r = f_{exp} - f_{th}$ versus pump wavelength for the same fit as panel (d).

In the preceding text, we prove that the phase distribution is transferred from the fundamental electric field to the nonlinear field based on the nonlinear interaction. Moreover, because phase-matching constraints are relaxed in flat optics, the transverse momentum (wave-vector) is likewise transferred. Figure 6 reveals this momentum transfer in SFG focusing. We introduce an x-directed tilt on the signal beam and compare it with normal (straight) incidence via observing the SHG of the signal beam [Figs. 6(b) and 6(d)]. Accordingly, with the pump beam incident normally, the SFG emission is focused on-axis for an untilted signal [Fig. 6(a)] and shifts to a corresponding tilt when the signal beam is tilted [Fig. 6(c)]. This behavior evidences momentum transfer in the nonlinear process and thus enables IR-to-visible image conversion while preserving most of the incident momentum information.

Via utilizing the nonlinear focusing of our proposed optical system, the infrared image can be transformed into the visible, allowing for it to be imaged and detected by a visible camera. The input signal at a given wavelength is then transformed via SFG and focused at a specific position according to Eq. (4), enabling the corresponding imaging plane to be located at different positions, as illustrated in Fig. 7(a). An imaging target, number "2," is placed in the signal arm for imaging. The signal wavelength is tuned from 800 to 1200 nm. The transformed number "2" images detected by a CMOS scientific camera are illustrated in Figs. 7(b)–7(f), with color indicating the SFG wavelength positions. The size of number "2" varies with the position of the imaging plane, due to changes in magnification caused by the tuned focal lengths. Consequently, we achieve the direct conversion of infrared images into visible and locate the imaging planes according to the signal wavelength, demonstrating an initial step toward multispectral nonlinear imaging.

3 Conclusion

In summary, we demonstrate dynamic nonlinear focusing enabled by phase transfer in second-order nonlinear interactions. By modulating the pump beam with an FZL phase distribution using an SLM, the phase is transferred to the generated SHG and SFG fields in a lithium niobate film, resulting in controllable nonlinear focusing. The focal length can be tuned through either the wavelength or the imposed phase distribution. We further show that transverse momentum is transferred from the fundamental field to the nonlinear emission. Building on this mechanism, we demonstrate a broadband infrared imaging approach by placing an imaging target in the signal arm. Because the focal length varies with the signal wavelength, infrared images at different wavelengths are formed at different imaging planes.

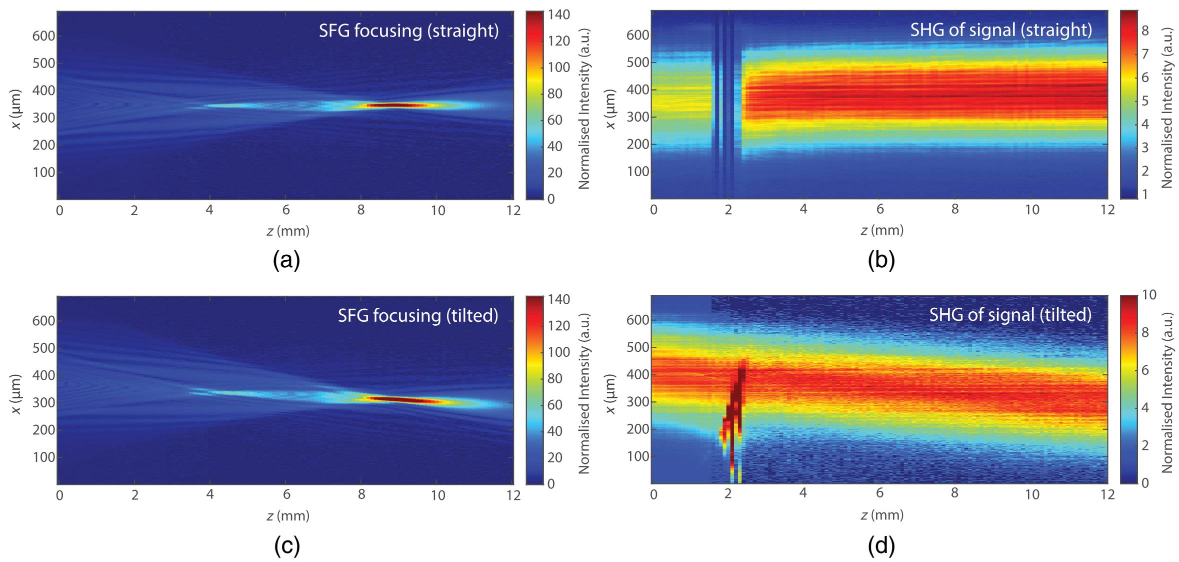

Fig. 6 Measured intensity distributions of the optical field in the *xz* plane of the SFG focusing and the SHG of the signal incidence under the normal (a), (b) and tiled (c), (d) incidence of the signal. The first half-wave zone has a radius of 120 pixels on the SLM in the FZL phase pattern. The signal wavelength and pump wavelength are fixed at 1100 and 1550 nm, respectively. The intensity was obtained from camera photon counts, corrected for background and normalized by the exposure time, and is therefore shown in relative units. The color scale is chosen to optimize overall visibility in each subfigure. As a result, the focal region may appear saturated.

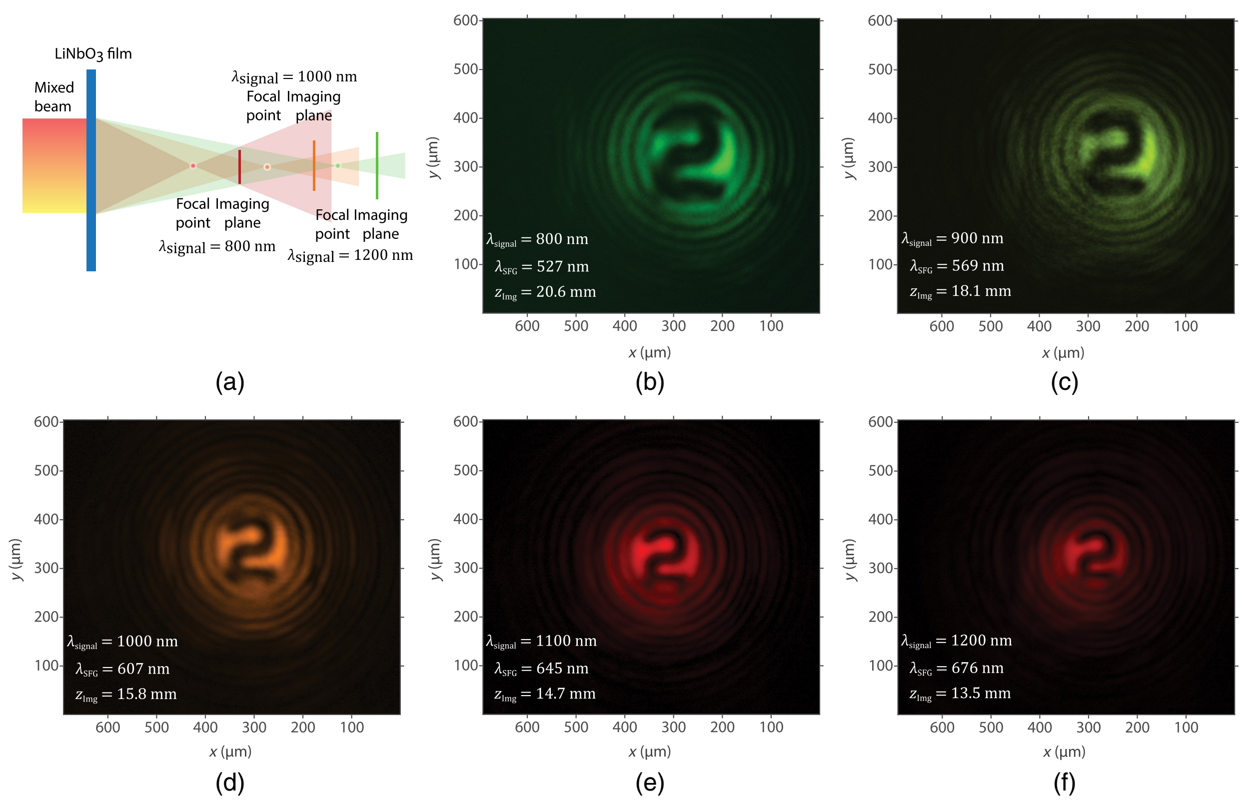

Fig. 7 (a) Schematic illustration of the multispectral IR imaging. (b)–(f) The converted number "2" images captured by a CMOS scientific camera with different signal wavelengths: (b) $\lambda_{\text{signal}} = 800$ nm, (c) $\lambda_{\text{signal}} = 900$ nm, (d) $\lambda_{\text{signal}} = 1000$ nm, (e) $\lambda_{\text{signal}} = 1100$ nm, and (f) $\lambda_{\text{signal}} = 1200$ nm. Here, the colors are used to exhibit the SFG radiation spectrum positions. The information on the incident signal wavelength, the SFG emission wavelength, and the position of the imaging plane is shown in the bottom left corner of panels (b)–(f).

These results highlight the role of phase and momentum transfer in nonlinear flat optics and open new opportunities for programmable and multispectral imaging.

Code and Data Availability

The code and data that support the findings of this study are publicly available on GitHub: https://github.com/advoptphotonicslab/VirtualLens.

Acknowledgments

This work was funded by the European Union (ERC, UPIRI, Grant No. 101170298). Views and opinions expressed are, however, those of the authors only and do not necessarily reflect those of the European Research Council. Neither the European Union nor the granting authority can be held responsible for them. G.Z. acknowledges the National Key Research and Development Program of China (Grant No. 2022YFA1404604). Z.Z. and M.R. acknowledge the support from the UK Research and Innovation Future Leaders Fellowship (Grant No. MR/Z000270/1). The authors acknowledge the use of NTU High-Performance Computing Cluster Avicenna.

References

1. B. B. Lahiri et al., "Medical applications of infrared thermography: a review," *Infrared Phys. Technol.* **55**(4), 221–235 (2012).
2. P. R. Norton, "Infrared image sensors," *Opt. Eng.* **30**(11), 1649–1663 (1991).
3. A. M. Waxman et al., "Color night vision: opponent processing in the fusion of visible and IR imagery," *Neural Networks* **10**(1), 1–6 (1997).
4. R. Gade and T. B. Moeslund, "Thermal cameras and applications: a survey," *Mach. Vis. Appl.* **25**(1), 245–262 (2014).
5. A. Kylili et al., "Infrared thermography (irt) applications for building diagnostics: a review," *Appl. Energy* **134**, 531–549 (2014).
6. S. Bianconi and H. Mohseni, "Recent advances in infrared imagers: toward thermodynamic and quantum limits of photon sensitivity," *Rep. Prog. Phys.* **83**(4), 044101 (2020).
7. A. Rogalski et al., "Infrared hot photodetectors: status and outlook," *Sensors* **23**(17), 7564 (2023).
8. A. Rogalski, "Infrared detectors: status and trends," *Prog. Quantum Electron.* **27**(2–3), 59–210 (2003).
9. R. Camacho-Morales et al., "Infrared upconversion imaging in nonlinear metasurfaces," *Adv. Photonics* **3**(3), 036002 (2021).
10. K. Huang et al., "Wide-field mid-infrared single-photon upconversion imaging," *Nat. Commun.* **13**(1), 1077 (2022).
11. Z. Zheng et al., "Third-harmonic generation and imaging with resonant Si membrane metasurface," *Opto-Electron. Adv.* **6**(8), 220174-1 (2023).
12. Z. Zheng et al., "Broadband infrared imaging governed by guided-mode resonance in dielectric metasurfaces," *Light: Sci. Appl.* **13**(1), 249 (2024).
13. P. Franken et al., "Generation of optical harmonics," *Phys. Rev. Lett.* **7**(4), 118–119 (1961).
14. R. W. Boyd, A. L. Gaeta, and E. Giese, "Nonlinear optics," in *Springer Handbook of Atomic, Molecular, and Optical Physics*, pp. 1097–1110, Springer (2008).
15. V. G. Dmitriev, G. G. Gurzadyan, and D. N. Nikogosyan, *Handbook of Nonlinear Optical Crystals*, Vol. 64, Springer (2013).
16. G. P. Agrawal, "Nonlinear fiber optics: its history and recent progress," *J. Opt. Soc. Am. B* **28**(12), A1–A10 (2011).
17. G. P. Agrawal, "Nonlinear fiber optics," in *Nonlinear Science at the Dawn of the 21st Century*, pp. 195–211, Springer (2000).
18. Q. Lin, O. J. Painter, and G. P. Agrawal, "Nonlinear optical phenomena in silicon waveguides: modeling and applications," *Opt. Express* **15**(25), 16604–16644 (2007).
19. R. Luo et al., "Semi-nonlinear nanophotonic waveguides for highly efficient second-harmonic generation," *Laser Photonics Rev.* **13**(3), 1800288 (2019).
20. R. L. Espinola et al., "Raman amplification in ultrasmall silicon-on-insulator wire waveguides," *Opt. Express* **12**(16), 3713–3718 (2004).
21. M. M. Fejer et al., "Quasi-phase-matched second harmonic generation: tuning and tolerances," *IEEE J. Quantum Electron.* **28**(11), 2631–2654 (2002).
22. P. Vabishchevich and Y. Kivshar, "Nonlinear photonics with metasurfaces," *Photonics Res.* **11**(2), B50–B64 (2023).
23. M. Rahmani et al., "Nonlinear frequency conversion in optical nanoantennas and metasurfaces: materials evolution and fabrication," *Opto-Electron. Adv.* **1**(10), 180021–180021 (2018).
24. C. Gigli and G. Leo, "All-dielectric $\chi(2)$ metasurfaces: recent progress," *Opto-Electron. Adv.* **5**(7), 210093-1 (2022).
25. A. Krasnok, M. Tymchenko, and A. Alù, "Nonlinear metasurfaces: a paradigm shift in nonlinear optics," *Materials Today* **21**(1), 8–21 (2018).
26. E. Almeida, G. Shalem, and Y. Prior, "Subwavelength nonlinear phase control and anomalous phase matching in plasmonic metasurfaces," *Nat. Commun.* **7**(1), 10367 (2016).
27. A. Pors, M. G. Nielsen, and S. I. Bozhevolnyi, "Analog computing using reflective plasmonic metasurfaces," *Nano Lett.* **15**(1), 791–797 (2015).
28. Y. Zhou et al., "Flat optics for image differentiation," *Nat. Photonics* **14**(5), 316–323 (2020).
29. D. de Ceglia et al., "Analog image processing with nonlinear nonlocal flat optics," *Opt. Mater. Express* **14**(1), 92–100 (2023).
30. H. Gao et al., "Recent advances in optical dynamic meta-holography," *Opto-Electron. Adv.* **4**(11), 210030-1 (2021).
31. M. Cotrufo et al., "Nonlinear analog processing with anisotropic nonlinear films," *Nanophotonics* **14**, 4099–4112 (2025).
32. V. V. Fedorov et al., "Gallium phosphide nanowires in a free-standing, flexible, and semitransparent membrane for large-scale infrared-to-visible light conversion," *ACS Nano* **14**(8), 10624–10632 (2020).
33. M. J. Booth, "Adaptive optical microscopy: the ongoing quest for a perfect image," *Light: Sci. Appl.* **3**(4), e165–e165 (2014).
34. Q. Zhang et al., "Adaptive optics for optical microscopy," *Biomed. Opt. Express* **14**(4), 1732–1756 (2023).
35. P. Hong et al., "Long-range correlation of transmitted light through transmission eigenchannels in disordered media," *Phys. Rev. B* **111**(2), 024202 (2025).
36. V. Nikolenko et al., "Slm microscopy: scanless two-photon imaging and photostimulation using spatial light modulators," *Front. Neural Circuits* **2**, 393 (2008).
37. O. Hernandez et al., "Three-dimensional spatiotemporal focusing of holographic patterns," *Nat. Commun.* **7**(1), 11928 (2016).
38. O. H. Karabey, *Electronic Beam Steering and Polarization Agile Planar Antennas in Liquid Crystal Technology*, Springer Science & Business Media (2013).
39. W. C. Goltsos and M. Holz, "Agile beam steering using binary optics microlens arrays," *Opt. Eng.* **29**(11), 1392–1397 (1990).
40. Y. Yang, A. Forbes, and L. Cao, "A review of liquid crystal spatial light modulators: devices and applications," *Opto-Electron. Sci.* **2**(8), 230026-1 (2023).
41. J. Rosen et al., "Roadmap on computational methods in optical imaging and holography," *Appl. Phys. B* **130**(9), 166 (2024).
42. G. Barbastathis, A. Ozcan, and G. Situ, "On the use of deep learning for computational imaging," *Optica* **6**(8), 921–943 (2019).
43. P. Hong, Y. Liang, and G. Zhang, "Robust multiple focusing through scattering media via feedback wavefront shaping," *Opt. Laser Technol.* **176**, 110939 (2024).
44. T. Fu et al., "Optical neural networks: progress and challenges," *Light: Sci. Appl.* **13**(1), 263 (2024).

45. S. N. Khonina et al., "Exploring types of photonic neural networks for imaging and computing—a review," *Nanomaterials* **14**(8), 697 (2024).
46. D. E. Zelmon, D. L. Small, and D. Jundt, "Infrared corrected sellmeier coefficients for congruently grown lithium niobate and 5 mol.% magnesium oxide–doped lithium niobate," *J. Opt. Soc. Am. B* **14**, 3319–3322 (1997).
47. I. Shoji et al., "Absolute scale of second-order nonlinear-optical coefficients," *J. Opt. Soc. Am. B* **14**, 2268–2294 (1997).
48. Y.-T. Qiu, L.-H. Hong, and Z.-Y. Li, "Rigorous solution to second harmonic generation considering transmission and reflection of light at air–crystal interface," *Chin. Phys. B* **32**(5), 050301 (2023).
49. L. Novotny and B. Hecht, *Principles of Nano-Optics*, 2nd ed., Cambridge University Press (2012).
50. R. W. Wood, *Physical Optics*, Macmillan (1905).

Ze Zheng is a research fellow at Nottingham Trent University (NTU), UK. He obtained his bachelor's degree from the School of Physics, Nankai University, in 2021 and his PhD, funded by the Royal Society, from the Department of Engineering, NTU, in 2025. He serves as a founder and officer of the International Society of Optics and Photonics (SPIE) student chapter at NTU. His main research areas include modelling and complex characterisations of dielectric metasurfaces for imaging and sensing applications.

Olga Sergaeva is a postdoctoral researcher in the Department of Information Engineering at the University of Brescia, Italy. She previously completed a postdoctoral fellowship at the University of Missouri, Columbia, MO, USA, from 2016 to 2018. Her research interests include nanophotonics, nonlinear optics, and ultrafast light–matter interaction.

Davide Rocco received his BSc degree in electronics and telecommunications engineering, his MSc degree in communication technologies and multimedia, and his PhD in information engineering from the University of Brescia, Italy, in 2012, 2015, and 2019, respectively. He is currently an associate professor with the Department of Information Engineering, University of Brescia. His research interests include integrated photonics, silicon photonics, microwave photonics, metasurfaces, and advanced photonic devices for communications and sensing applications.

Yuchen Zhang received her BS degree in physics from Liaoning Normal University, China, and his PhD in optics from Nankai University, China, in 2017 and 2024, respectively. She is currently a lecturer with the School of Science, Tianjin Chengjian University, China. Her research focuses on micro- and nano-optoelectronic devices based on ferroelectric materials.

Guoquan Zhang received his BSc, MSc degrees, and PhD in the School of Physics of Nankai University, China, in 1993, 1995, and 1998, respectively. He is currently a professor at the School of Physics, Nankai University. His research interests include integrated photonics, nonlinear optics, and quantum optics.

Mohsen Rahmani obtained his PhD from the National University of Singapore (2013), followed by a postdoc at Imperial College London and a DECRA Fellowship at the Australian National University. In 2020, he joined NTU via the Royal Society Wolfson Fellowship, followed by the UKRI Future Leaders Fellowship and ERC Consolidator Grant. He is the past chair of the IEEE Nanotechnology Chapter across the UK and Ireland section. His research activities span over the metasurface design and applications in non-linear imaging, bio-sensing, and reconfigurable optics.

Costantino De Angelis received his PhD from the University of Padova (1993), where he served as an assistant professor of Electromagnetic Fields and Photonics. In 1998, he joined Brescia University where he has been a full professor of Electromagnetic Fields and Photonics since 2004. He is the head of the NORA group at the University of Brescia (https://nora.unibs.it/home), and his current research interests include nonlinear optics, nanophotonics, and optical metamaterials.

Lei Xu obtained his PhD from Nankai University in 2014, followed by postdocs at Nankai University, the Australian National University, and the University of New South Wales. In 2020, he joined NTU. He is a past chair of the IEEE Nanotechnology Chapter across the UK and Ireland section, and a recipient of the inaugural SPIE Advanced Photonics Young Innovator Award-2025. His research interests include the modelling and verification of linear and nonlinear metasurfaces, optoelectronics meta-devices via machine learning, genetic algorithms, and other AI twin programs.